Conformational Behavior and Tautomer Selective Photochemistry in Low Temperature Matrices: The Case of 5-(1H-Tetrazol-1-yl)-1,2,4-triazole

6 AUTHORS, INCLUDING:

Magdalena Pagacz-Kostrzewa
University of Wroclaw
9 PUBLICATIONS **60** CITATIONS

SEE PROFILE

Igor D. Reva
University of Coimbra
126 PUBLICATIONS **2,549** CITATIONS

SEE PROFILE

Rui Fausto
University of Coimbra
330 PUBLICATIONS **4,517** CITATIONS

SEE PROFILE

Maria Wierzejewska
University of Wroclaw
61 PUBLICATIONS **475** CITATIONS

SEE PROFILE

Conformational Behavior and Tautomer Selective Photochemistry in Low Temperature Matrices: The Case of 5-(1H-Tetrazol-1-yl)-1,2,4-triazole

M. Pagacz-Kostrzewa,[†] I. D. Reva,*,[‡] R. Bronisz,[†] B. M. Giuliano,[‡] R. Fausto,[‡] and M. Wierzejewska*,[†]

[†]Faculty of Chemistry, University of Wrocław, Joliot-Curie 14, 50-383 Wrocław, Poland
[‡]Department of Chemistry, University of Coimbra, 3004-535 Coimbra, Portugal

S *Supporting Information*

ABSTRACT: The conformational properties and the photolysis behavior of one of the simplest N—C bonded bicyclic azoles, 5-(1H-tetrazol-1-yl)-1,2,4-triazole (**T**), were studied in argon and xenon matrices by infrared spectroscopy. Analysis of the experimental results was supported by extensive theoretical calculations carried out at the B3LYP/6-311++G(2d,2p) level of approximation. Out of the eight **T** minima located on the potential energy surface, the three most stable species were detected in low temperature matrices, namely, 5-(1H-tetrazol-1-yl)-1H-1,2,4-triazole (**T1**) and two conformers of 5-(1H-tetrazol-1-yl)-2H-1,2,4-triazole (**T2a** and **T2b**). With increase of the substrate temperature either during deposition of the matrices or during annealing the **T2b → T2a** conversion took place, in agreement with the predicted low energy barrier for this transformation (5.38 kJ mol^{-1}). Both broad band and narrow band laser UV irradiations of **T** isolated in Xe and Ar matrices induce unimolecular decomposition involving cleavage of the tetrazole ring of **T1** and **T2a** (**T2b**) that leads to the production of 1H-1,2,4-triazol-5-yl carbodiimide (**P1**) and 1H-1,2,4-triazol-3-yl carbodiimide (**P2**), respectively. When the laser is used, in addition to the main **P1** and **P2** photoproducts, several minor products could be successfully identified in the matrices: N-cyanocarbodiimide HNCNCN (detected for the first time) associated with nitrilimine HNNCH and HCN. An interesting phenomenon of tautomer-selective photochemistry was observed for the matrix-isolated compound. It could be explained by the different LUMO—HOMO energy gaps estimated for **T1**, **T2a**, and **T2b**, connected with different threshold energies necessary to start the photolysis of **T1** and **T2a** (**T2b**).
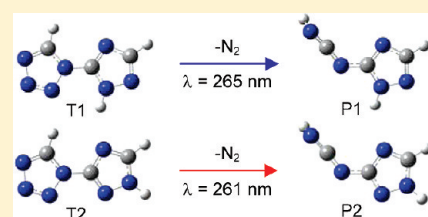
INTRODUCTION

Tetrazole and triazole derivatives, as well as bicyclic azoles, find wide application in many fields, such as medicine, agriculture, and high-energy materials. They represent one of the most biologically active classes of compounds and receive many applications in the synthesis of potent medicines with diverse pharmacological activity.[1−5] Five-membered nitrogen-containing heterocycles are also traditional sources of energetic materials.[6−8] It was shown recently that the N—C bonded bicyclic azoles not only are highly energetic but also tend to be thermally more stable than their monoazole analogues.[9,10] A number of metal coordination compounds with bisazole ligands appeared to show novel topologies for application in supramolecular chemistry or exhibit interesting magnetic properties, including spin crossover.[11−17]

From the fundamental point of view, triazole and tetrazole derivatives have been found to be very interesting and challenging molecules because they usually possess different tautomers and/or conformers[18−24] and they might be expected to have rich, strongly dependent on the substituents, photochemistry.[22,25−34]

The subject of this study, 5-(1H-tetrazol-1-yl)-1,2,4-triazole (**T**),[35] is one of the simplest N—C bonded bicyclic azoles. Contrary to 3,4′-bi(1,2,4-triazole) and 5,5′-bitetrazole, whose crystal structures have been reported,[36,37] the title molecule was

not the subject of any previous X-ray or spectroscopic investigation. In addition, although the photochemistry of tetrazole derivatives has been the subject of a number of studies, mostly under matrix isolation conditions, photolysis of simple bicyclic azoles was not investigated until now.

The aim of the present work was to study both the conformational behavior of 5-(1H-tetrazol-1-yl)-1,2,4-triazole and its UV-induced phototransformations. We used matrix isolation FTIR spectroscopy as the main experimental analytical tool to take advantage of its unique capabilities for such studies. Indeed, for a matrix-isolated compound, it is possible to achieve an essential simplification of the spectra and high spectroscopic resolution, allowing spectral signatures of different tautomers or conformers to be distinguished. In addition, for matrix isolated species, unimolecular photochemistry is expected, with the products being cage-confined. Since molecular diffusion in the solid low temperature matrices is in general inhibited, no cross reactions usually take place involving species resulting from different precursor molecules. Such simplification is very useful for mechanistic elucidation. The interpretation of the experimental results was supported by extensive B3LYP/6-311++G(2d,2p)

calculations on possible **T** tautomers and conformers as well as on expected photochemistry products.

■ EXPERIMENTAL AND COMPUTATIONAL METHODS

Synthesis of 5-(1H-Tetrazol-1-yl)-1,2,4-triazole. A mixture of sodium azide (7.8 g, 0.12 mol), 3-amino-1H-1,2,4-triazole (7.0 g, 0.10 mol), triethylorthoformate (22 mL, 0.13 mol), and glacial acetic acid (50 mL) was refluxed for 24 h. Next, a concentrated hydrochloric acid (12 mL) was added. The precipitated sodium chloride was filtered off and the filtrate was concentrated using a rotary evaporator. The obtained residue was dissolved in boiling ethanol and the hot solution was filtered. After the obtained solution was allowed to cool, the solid matter was filtered off. The obtained crude product was recrystallized from boiling water. Yield 7.0 g (51%) of colorless thin needles. Anal. Found (M_w = 137.10): C, 26.2; H, 2.1; N, 72.3. Calcd for $C_3H_3N_7$: C, 26.3; H, 2.2; N,71.5. ^{1}H NMR (300 MHz, DMSO-d_6, 298 K): 8.86 (s, 1H), 10.09 (s, 1H), 14.82 (wide singlet, 1H) ppm. ^{13}C NMR (300 MHz, DMSO-d_6, 298 K): 153.2, 146.4, 143.9 ppm.

The ^{1}H and ^{13}C NMR spectra were recorded using a Bruker Aspect AM300 spectrometer at room temperature in DMSO-d_6 solutions. Elemental analyses for carbon, hydrogen, and nitrogen were performed on a VarioEL III CHNS analyzer. All reagents were commercially available and used without further purification.

Matrix Isolation Studies. In order to prepare matrices containing **T**, the crystalline sample was allowed to sublime from a small electric oven placed inside the vacuum chamber of the cryostat. The obtained **T** vapors were codeposited with a large excess of argon or xenon onto the CsI window kept at 13 or 15 K (Ar) and 15 or 30 K (Xe). Cryogenic temperatures were obtained by means of an APD Cryogenics close-cycle refrigeration system with a DE-202A expander. The temperature was measured directly at the sample holder by a silicon diode sensor working with a digital controller (Scientific Instruments, model 9650-1).

Matrices were irradiated with a 300 W output power of a Xe/Hg arc lamp (Oriel, Newport), using a series of long-pass and band-pass optical filters transmitting UV light with λ >367, λ >328, λ >288, and λ >234 nm. The UV cutoff edge of these filters is characterized by 40% transmittance at the specified wavelength, allowing for a small portion of higher energy radiation to pass through. The optical characteristics for one of the most important filters used in this work (bandpass, λ >288) were similar to the U11 UV glass. Matrices were irradiated also with tunable UV light provided by the frequency doubled signal beam of a Quanta-Ray MOPO-SL pulsed (10 ns) optical parametric oscillator (fwhm ~0.2 cm^{-1}, repetition rate 10 Hz, pulse energy ~1.0 mJ) pumped with a pulsed Nd:YAG laser.

The IR spectra were recorded with 0.5 cm^{-1} resolution using a Nicolet 6700 Fourier transform infrared spectrometer equipped with a DTGS detector and a Ge/KBr beamsplitter.

Computational Details. All calculations were performed with the Gaussian 03 program package.[38] Structures of the minima and transition states were optimized at the B3LYP/6-311++G-(2d,2p) level. The associated force constant matrices were calculated at the same level of theory to evaluate harmonic frequencies and zero-point vibrational (ZPE) corrections. The DFT calculated wavenumbers were scaled down to account for anharmonicity effects by 0.945, above 2800 cm^{-1}, and by 0.984, between 2800 and 400 cm^{-1}. Potential energy distributions (PEDs) of the normal modes were computed with the GAR2PED program,[39] and vibrational spectra were simulated
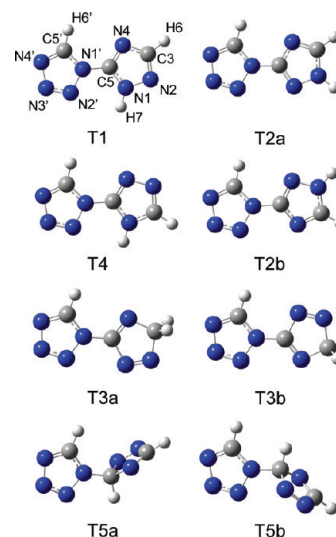

Figure 1. B3LYP/6-311++G(2d,2p) optimized structures of the **T** isomers.

using SYNSPEC.[40] The influence of a polar environment on the stability order of the most stable **T** isomers was estimated using the conductor-like polarized continuum CPCM approach in water solution at the B3LYP/6-311++G(2d,2p) level.[41,42] Energies of the low-energy excited states were calculated using the time-dependent density functional theory (TD-DFT).[43,44]

■ RESULTS AND DISCUSSION

DFT Calculations. *Structures and Relative Energies of the Minima.* The 5-(1H-tetrazol-1-yl)-1,2,4-triazole molecule (**T**) may exist in three tautomeric forms, differing by the position of the H atom connected to N in the triazole ring. A priori, for each tautomer different conformers can be conceived with different mutual arrangements of the triazole and tetrazole rings. According to the performed B3LYP/6-311++G(2d,2p) calculations, four low energy minima exist (Figure 1). The global minimum is **T1**, which possesses the annular H7 atom attached to the N1 atom of the triazole ring and is stabilized by the favorable interaction of this hydrogen with the N2$'$ atom of the tetrazole ring. The next two structures in order of stability are two different conformers of the tautomeric species with the annular proton connected to N2, differing from each other by the relative arrangement of the rings: **T2a** and **T2b** are 3.65 and 6.92 kJ mol^{-1} higher in energy than the most stable structure, respectively. The least stable of the four low-energy minima is tautomer **T4**, with the triazole-ring hydrogen atom in position N4 and the relative energy of 24.6 kJ mol^{-1}. Three of the four mentioned minima are planar structures (C_s symmetry) and one (**T2b**) is nonplanar (C_1 symmetry) with the N2$'$−N1$'$−C5−N4 dihedral angle of 14.9°. The absence of the two additional local minima (**T1b** and **T4b**) that might be designed for **T1** and **T4** tautomers by analogy with the **T2a**/**T2b** pair deserves further comment. Figure 2 shows the relaxed potential energy scans for the internal rotation of the tetrazole and triazole rings (around the N1$'$−C5 bond) calculated at the B3LYP/6-311++G(2d,2p) level for the three **T** tautomers. The shape of these profiles, with only one minimum for **T1** and **T4** and with two minima for **T2**, clearly justifies the lack of these local minima in the case of the **T1** and **T4** tautomers.

The calculations revealed also the existence of two pairs of conformers of high energy isomers of the compound, (T3a, T3b) and (T5a, T5b), in which the annular hydrogen is connected to the C3 or C5 atoms, respectively. In these species, either C3 or C5 exists in the sp^3 hybridization state, resulting in the loss of the triazole ring aromaticity and the consequent decrease of stability. Indeed, T3a, T3b, T5a and T5b forms are characterized by very high relative energies (over 120 kJ mol^{-1}). A set of the calculated geometric parameters for the most stable T minima is given in Table S1, in the Supporting Information.

Structures and Energies of the Transition States. Nine transition states (TS) have been located on the potential energy surface, allowing for the estimation of the energy barriers
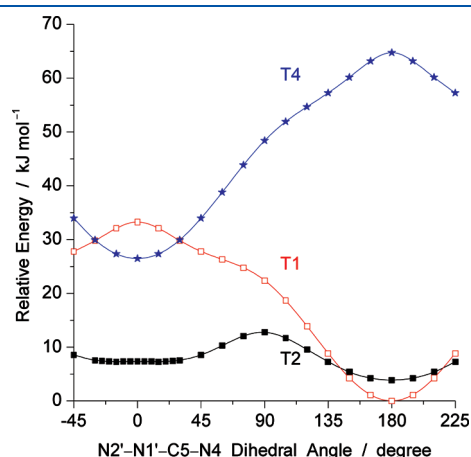

Figure 2. Relaxed potential energy scans for the internal rotation of the tetrazole and triazole rings calculated at the B3LYP/6-311++G(2d,2p) level of theory for the three tautomers of T. The calculated values of E and E_{ZPE} for the most stable conformer T1 are equal to −499.453843 and −449.367337 hartree, respectively.

between the different T species. The respective ZPE corrected potential energy diagram is presented in Figure 3.

The most stable form T1 may isomerize to tautomer T2a by direct [1,2]-hydrogen transfer between two adjacent nitrogen atoms via transition state TS1, with a high energy barrier of 212 kJ mol^{-1}. TS1 has a strongly elongated N1−N2 bond (1.472 Å) as compared with those found in T1 and T2a (1.358 and 1.355 Å, respectively). The migrating H atom is situated out of the ring plane and takes the intermediate position between N1 and N2. In turn, interconversion between conformers T2a and T2b involves rotation of the rings and is associated with a change of the N2′−N1′−C5−N4 dihedral angle. This process requires an activation energy of 8.65 kJ mol^{-1} (in the direction T2a → T2b) and proceeds via TS2, where the N2′−N1′−C5−N4 angle equals 88.3°, as compared to those calculated for the minima: 180.0° (T2a) and 14.9° (T2b). Direct interconversion between T2b and the most stable T1 form is not possible. Starting from T2b, a two-step route is possible to obtain tautomer T4, involving consecutive N2 → C3 and C3 → N4 H-shifts within the triazole ring. The interconversion proceeds via TS3 and TS4, with the high energy nonaromatic isomer T3b as an intermediate product. The energy barriers for the T2b → T3b and T3b → T4 transformations are equal to 219 and 135 kJ mol^{-1}, respectively. There are several other pathways available involving the higher energy isomers. T3a, T5a, and T5b may be formed from T2a, T1, and T4, respectively, via TS6, TS5, and TS7 transition states, which are characterized by high relative energies, exceeding 250 kJ mol^{-1}, and thus forcing high energy barriers for these transformations. Much less energy is required for the T5a ↔ T5b and T3a ↔ T3b interconversions.

Population of the Tautomers and Conformers of T. Assuming at first that the equilibrium between the T minima is achieved in the gas phase, the calculated abundance at 298 K of the three most stable species (T1, T2a, and T2b) equals 65.7, 25.0, and 9.3%, respectively. The remaining structures have a negligible
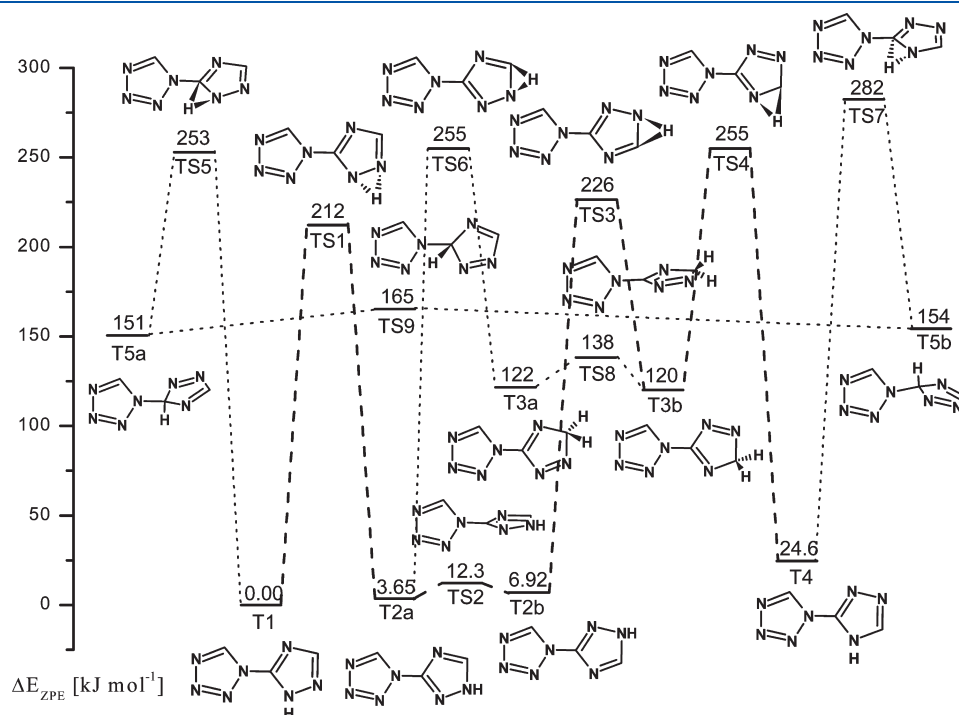

Figure 3. B3LYP/6-311++G(2d,2p) ZPE corrected potential energy diagram for T isomerizations.

Table 1. Relative Energies ΔE, Zero-Point Energy Corrected Relative Energies ΔE_{ZPE}, Relative Gibbs Free Energies ΔG_{298} (kJ mol^{-1}), and Abundances A_{298} and A_w (%)^a for Different T Isomers and Transition States Calculated at the B3LYP/6-311++G(2d,2p) Level

minima	ΔE	ΔE_{ZPE}	ΔG_{298}	A_{298}	A_w
T1	0.00	0.00	0.00	65.7	57.1
T2a	3.90	3.65	2.39	25.0	26.3
T2b	7.32	6.92	4.85	9.30	16.6
T4	26.5	24.6	24.4	0.00	0.00
T3a	128	122	121	0.00	0.00
T3b	126	120	120	0.00	0.00
T5a	156	151	149	0.00	0.00
T5b	160	154	153	0.00	0.00

transition states	ΔE	ΔE_{ZPE}	ΔG	ν_i
TS1	230	212	212	1752i
TS2	12.8	12.3	15.3	47i
TS3	242	226	226	1422i
TS4	272	255	254	1519i
TS5	269	253	252	1431i
TS6	244	228	228	1425i
TS7	299	282	280	1487i
TS8	145	138	141	69i
TS9	171	165	168	61i

^{a} A_{298}, calculated gas phase abundance at 298 K; A_w, abundance estimated from the experimental band intensities weighted by the theoretically calculated IR intensities. The calculated values of E, E_{ZPE}, and G_{298} for the most stable conformer (T1) are equal to -499.453843, -499.367337, and -499.399930 hartree, respectively.

Figure 4. Relaxed potential energy scan for the internal rotation of the tetrazole and triazole rings calculated at the B3LYP/6-311++G(2d,2p) level of theory for **T2** tautomer. The relative zero energy corresponds to the energy of tautomer **T1**. The horizontal line around **T2b** minimum shows the zero-point vibrational energy level related with the inter-ring torsion coordinate.

D1
$\Delta E_{ZPE} = 10.5$ kJ mol^{-1}

D2
$\Delta E_{ZPE} = 0.00$ kJ mol^{-1}

DTS
$\Delta E_{ZPE} = 62.9$ kJ mol^{-1}

Figure 5. B3LYP/6-311++G(2d,2p) optimized structures of the **T** dimers and the transition state joining them. All three species belong to the C_{2h} point group. The calculated values of E and E_{ZPE} for the most stable dimer (**D2**) are equal to -998.926538 and -998.752086 hartree, respectively.

population and are expected to be of no importance in relation to the experimental spectra. The relative energies, relative Gibbs free energies, and calculated abundances of all **T** minima are collected in Table 1. All three **T1**, **T2a**, and **T2b** structures were considered to contribute to the equilibrium with equal weights, although this seems to be in contradiction with their symmetries: **T1** and **T2a** belong to the C_s point group and should have the degeneracy of 1, while **T2b** belongs to the C_1 point group and should have a weight equal to 2. However, a closer inspection of the relaxed potential energy scan for the internal rotation in tautomer **T2** provides the explanation for the assumption of equal statistical weights for the three forms. It is presented in Figure 4 in an expanded scale as compared to the same profile in Figure 2. In the vicinity of N2′−N1′−C5−N4 equal to 0°, a large variation of the reaction coordinate (more than 50°) leads to a change in the relative energy that does not exceed 0.1 kJ mol^{-1} and stays below the zero-point vibrational energy. Thus, the effective symmetry of **T2b** may be regarded as C_s, justifying the degeneracy of **T2b** being the same as those of **T1** and **T2a**.

Nevertheless, the large value of the energy barrier for the unimolecular **T1** → **T2a** tautomerization (212 kJ mol^{-1} calculated at the B3LYP/6-311++G(2d,2p) level) implies that the true thermodynamic equilibrium at room temperature cannot be established in the gas phase between tautomers **T1** and **T2**. However, as discussed later, all of the three most stable species (**T1**, **T2a**, **T2b**) are present in inert matrices at 15 K (both in Ar and Xe). This fact is also in apparent contradiction with the expected tautomeric selectivity of the studied molecule
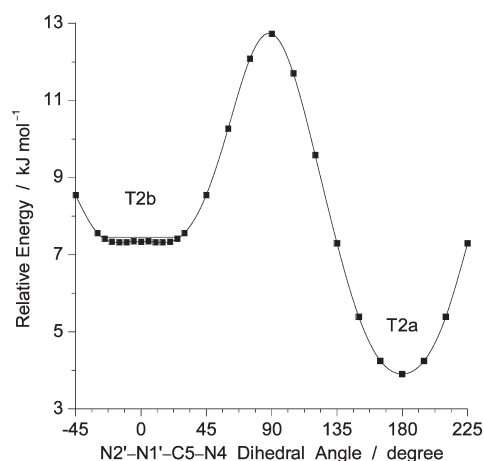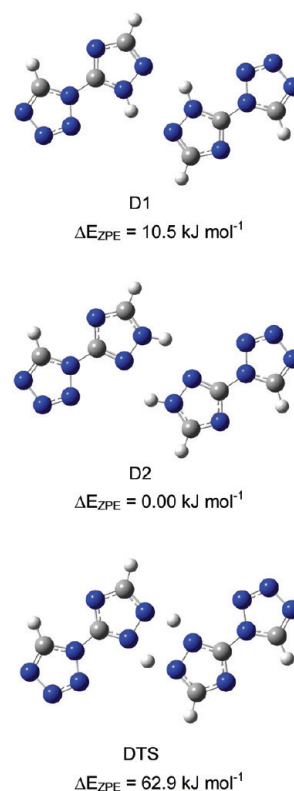
in the condensed phase. Indeed, usually the compounds amenable to tautomerism crystallize predominantly in one tautomeric form.[45−48] Unfortunately, there are no crystal data available for **T**. The compound crystallizes as thin needles, and it is difficult to
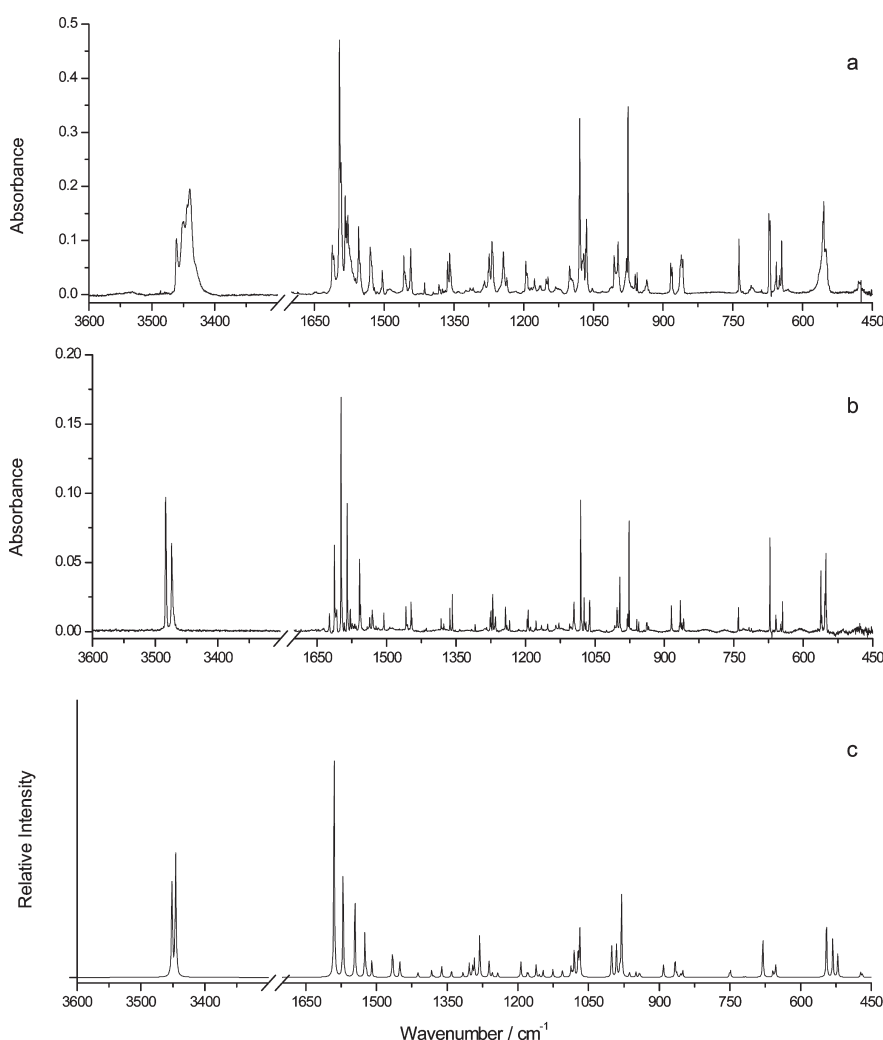
5696

dx.doi.org/10.1021/jp202925r | J. Phys. Chem. A 2011, 115, 5693–5707

Figure 6. IR spectra of T: (a) spectrum of **T** isolated in a freshly deposited Xe matrix at 15 K; (b) spectrum of **T** isolated in a freshly deposited Ar matrix at 15 K; (c) simulated sum spectrum obtained by adding the B3LYP/6-311++G(2d,2p) spectra of **T1**, **T2a**, and **T2b** isomers taken with the abundances estimated from band intensities weighted by the theoretically calculated IR intensities. The theoretical spectrum was created using Lorentzian functions centered at the calculated frequencies scaled as described in Experimental and Computational Methods and with the bandwidth at half-height equal to 1 cm^{-1} (1.5 cm^{-1} for the ν(NH) stretching region).

obtain crystals large enough to perform X-ray measurements. Nonetheless, whichever tautomeric form is realized in the crystals, either **T1** or **T2**, it does not explain the simultaneous experimental observation of **T1**, **T2a**, and **T2b** isolated in matrices. In order to be trapped in matrices, these three species must first be present in the gas phase obtained from sublimation of the crystalline sample. However, as mentioned above, the thermal equilibration between **T1** and **T2** monomers in the gas phase at room temperature is not possible due to the associated high energy barrier, so that only **T1** or **T2** should be trapped in the cryogenic matrices, depending on which tautomer is present in the crystal. Thus, another mechanism for tautomerization must take place *during* the sublimation of the solid sample.

A similar situation is known for the case of cytosine. It exists in crystals as the canonic amino—oxo tautomer.[48] However, in gas phase and in cryogenic matrices, cytosine assumes at least three different tautomeric forms.[49] The mechanism of cytosine tauto-merization has already been addressed by Yang and Rodgers.[50] These authors explained the coexistence in the gas phase of several cytosine tautomers, despite very high energy barriers

between them, by bimolecular tautomerization rising from the hydrogen bonded cytosine dimers in the crystal. Such hydrogen bonding interactions result in a significant lowering of the barriers to tautomerization that allows for the dimer dissociation in the gas phase with the production of new tautomers. The relevant case of 1-(tetrazolyl-5-yl)ethanol has been recently studied by Ismael et al.[51] where a considerably different relative population of the two tautomers of the molecule was found for the compound trapped in cryogenic matrices, compared to the theoretical predictions for the gas phase equilibrium situation at the thermodynamic reference temperature. In that case, the tautomer present in the crystalline phase before sublimation was known and the population of this tautomer found in the matrices was approximately twice that predicted for the equilibrium.[51]

To find an explanation for the observed coexistence of **T1**, **T2a**, and **T2b** species in the studied matrices (see following section), we followed the same approach as presented by Yang and Rodgers.[50] Figure 5 shows the optimized structures of the centrosymmetric dimers **D1** and **D2**, constructed from two **T1**
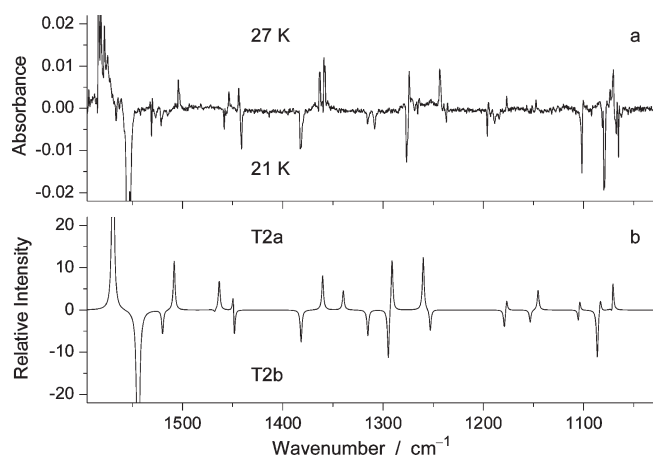
Figure 7. IR spectra of **T**: (a) experimental difference spectrum of **T** isolated in a xenon matrix, showing changes upon annealing occurring in the temperature interval from 21 to 27 K, the growing bands show upward; (b) simulated difference spectrum between the theoretically calculated spectra of **T2a** (positive bands) and **T2b** (negative bands) constructed as "T2a" *minus* "T2b".The theoretical spectra were simulated with Lorentzian functions (fwhm = 2 cm^{-1}) centered at the frequencies calculated at the B3LYP/6-311++G(2d,2p) level of theory and scaled by a factor of 0.984. The strongest absorptions are truncated in both frames.

and two **T2a** units, respectively. The structure of a second-order transition state, **DTS**, connecting these species and characterized by two imaginary frequencies describing antisymmetric and symmetric synchronous motions of the two labile protons is also presented. The calculated ZPE corrected relative energies of **D2**, **D1**, and **DTS** are equal to 0.00, 10.5, and 62.9 kJ mol^{-1}, respectively. In a similar way to cytosine,[50] the formation of dimers promotes a significant lowering of the barrier for the bimolecular tautomerization as compared to the unimolecular process (from 212 to 31.4 kJ mol^{-1}). Thus, the presence of the **T** dimers in the crystalline phase should facilitate tautomerization and formation of the new tautomers during the sublimation process. As already mentioned, the crystal structure of the studied compound was not published until now; however on the basis of X-ray studies performed for other azole derivatives, it is known that such molecules in the solid state usually form a hydrogen bonded network, which includes N–H···N hydrogen bond donating and accepting N atoms of the azole rings.[37,52]

Assuming that the tautomerization of **T** during sublimation is not governed by the Boltzmann statistics, the amount of each form in the matrices was estimated empirically, from the experimentally observed integrated band intensities weighted by the theoretically calculated IR intensities, and found to be equal to 57.1, 26.3, and 16.6%. Comparing the two sets of populations for **T**, equilibrium values derived from the theoretically calculated relative energies (65.7, 25, 9.3%) versus the experimentally derived values (57.1, 26.3, and 16.6%), one may suppose that the 2*H*-tautomer (**T2**) is present in the condensed state instead of the 1*H*-tautomer (**T1**). This prediction is in agreement with the calculated values of the relative energies of dimers **D1** and **D2** (see above) as well as monomers of **T** obtained within the CPCM model using water as solvent. Under such conditions, both **T2a** and **T2b** are more stable than **T1** by ca. 13 and 12 kJ mol^{-1} (ΔE values without ZPE corrections), respectively. Both **T2a** and **T2b** have very large molecular dipole

moments (over 8 D) comparing with **T1** (less than 3 D) and should be strongly stabilized in condensed media.

IR Spectrum of the Matrix Isolated T and Its Comparison with the Theoretical Predictions. *Xenon Matrices Deposited at 15 K.* Figure 6 (upper trace) presents the infrared spectrum of **T** embedded in a freshly deposited xenon matrix at 15 K. Closer inspection of this spectrum reveals, the presence of the three most stable **T1**, **T2a**, and **T2b** species. Indeed, the experimental spectrum fits well the theoretical sum spectrum obtained by adding the B3LYP/6-311++G(2d,2p) spectra of the three most stable **T** structures weighted by their respective abundances (see bottom trace in Figure 6).

As can be noticed from Figure 6, many bands in the experimental **T**/Xe spectrum appear split due to existence of different matrix sites. Extensive site splitting has been earlier observed for other tetrazole derivatives isolated in low temperature matrices.[27,53,54]

Among the most intense absorptions in the experimental spectrum are those due to the stretching and deformation modes of the N–H group of the triazole ring originating mainly from **T1** and **T2a** species. The ν(N–H) vibration of these species in solid xenon gives rise to the doublets of bands at 3444, 3440 (**T1**) and 3461, 3450 cm^{-1} (**T2a**) while the out-of-plane γ(NH) mode gives rise to a doublet at 555, 556 cm^{-1} (**T1**) and to a nonsplit band at 555 cm^{-1} (**T2a**). The region below 1550 cm^{-1} contains many relatively intense bands and reflects, in agreement with the PED matrices obtained for all **T1**, **T2a**, and **T2b** species (see Table S2 in the Supporting Information), the presence of strongly coupled triazole and tetrazole rings stretching and deformation modes, as it occurs for example in the case of the two most intense bands observed in this part of the spectrum, at 1080 and 976 cm^{-1}.

Annealing of Xenon Matrices Deposited at 15 K. Annealing of the xenon matrix deposited at 15 K led to the disappearance of the bands attributed to the least stable **T2b** conformer. The onset of this process was observed already at 21 K, and it continued during further heating. Simultaneously, the intensity of the bands originating from conformer **T2a** increased, showing that the **T2b** → **T2a** conversion was taking place. When the matrix temperature attained 36 K, all bands due to conformer **T2b** disappeared. Figure 7 shows the 1600–1050 cm^{-1} region of the experimental difference spectrum of **T** isolated in a xenon matrix, showing the changes occurring upon annealing in the temperature interval from 21 to 27 K. The simulated difference spectrum (**T2a** *minus* **T2b**) is also shown for comparison. The results indicate that the **T2b** tautomer is thermally unstable in a xenon matrix at elevated temperatures. The conclusion can be easily justified when one considers the theoretically predicted energy barrier for the **T2b** → **T2a** transformation (see Figure 3 and Table 1), which amounts only to 5.38 kJ mol^{-1} and may be easily overcome under the appropriate conditions of the matrix experiment.

It should be noted further that annealing permitted establishment of the experimental conditions (temperature of ca. 30 K) where the conformational composition of **T** could be reduced to only two structures. This conformational behavior of **T** was then used to simplify the photochemical experiments described later on in this paper. The xenon matrices intended for photochemical studies were deposited at 30 K and contained initially only **T1** and **T2a**.

Xenon Matrices Deposited at 30 K. When the IR spectrum of **T** isolated in a xenon matrix deposited at 30 K is considered, the
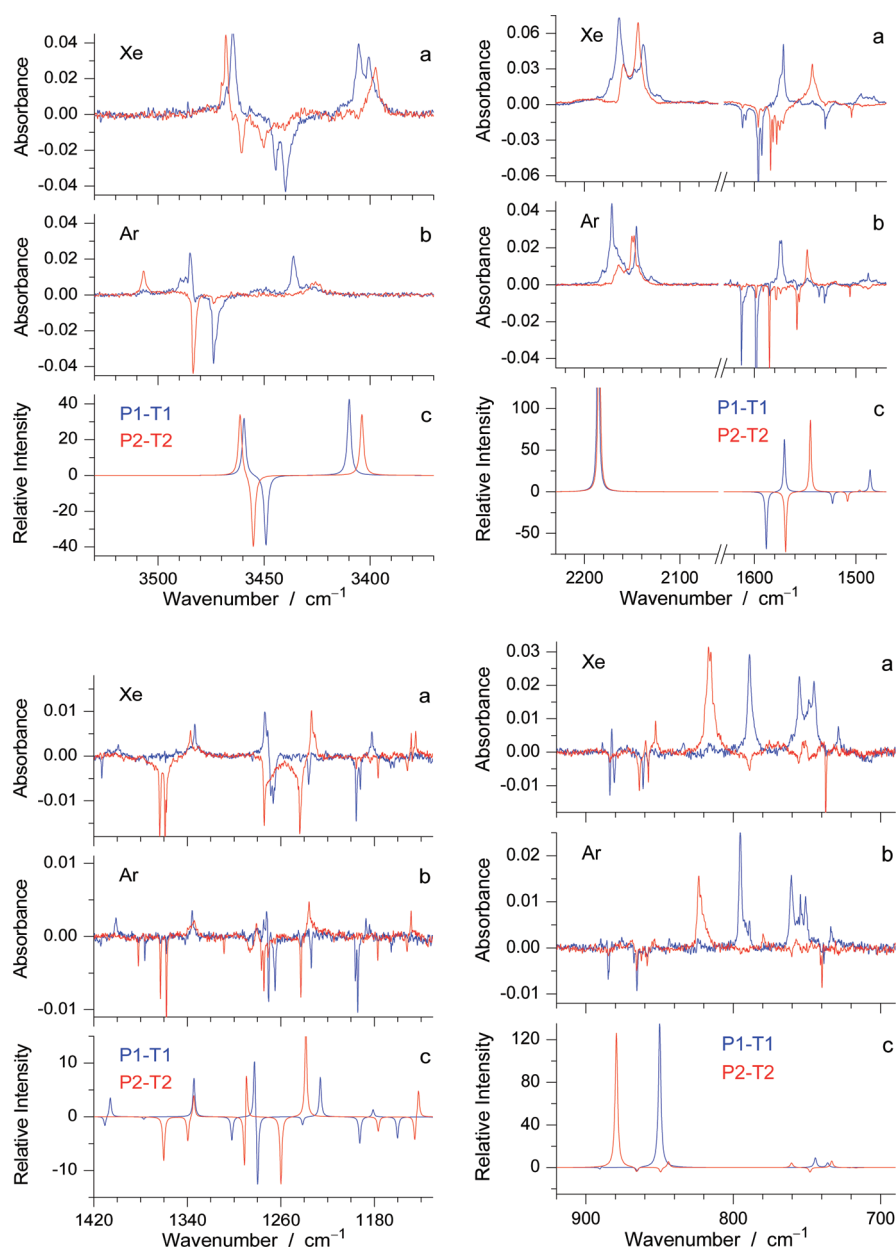
Figure 8. Selected regions of the spectra. (a) Experimental difference spectra of **T** isolated in a xenon matrix at 30 K: blue trace, changes after 15 min of irradiation by Xe/Hg arc lamp equipped with cutoff filter transmitting UV light with $\lambda > 288$ nm; red trace, changes after 25 min of additional irradiation by Xe/Hg arc lamp equipped with cutoff filter transmitting UV light with $\lambda > 234$ nm (subsequent to irradiation with $\lambda > 288$ nm). Growing bands show upward. (b) Experimental difference spectra of **T** isolated in an argon matrix at 13 K: blue trace, changes after 3 h of irradiation by Xe/Hg arc lamp equipped with cutoff filter transmitting UV light with $\lambda > 288$ nm; red trace, changes after 40 min of additional unfiltered irradiation by Xe/Hg arc lamp, through a quartz window of the cryostat (subsequent to irradiation with $\lambda > 288$ nm, followed by 20 min of irradiation with $\lambda > 234$ nm). Growing bands show upward. (c) Simulated difference spectra constructed as "**P1** minus **T1**" (blue trace) and "**P2** minus **T2a**" (red trace). The theoretical spectra were simulated with Lorentzian functions (fwhm = 2 cm^{-1}) centered at the frequencies calculated at the B3LYP/6-311++G(2d,2p) level of theory and scaled by factors of 0.945 (above 3000 cm^{-1}) and 0.984 (below 3000 cm^{-1}). Positive bands are due to **P1** (blue) and **P2** (red), negative bands are due to **T1** (blue) and **T2a** (red).
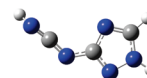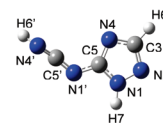
picture is similar to that observed after the annealing of the matrix deposited at 15 K. The experimental data fit well the sum spectrum predicted for only the two most stable **T1** and **T2a** species. Conformational cooling during deposition of a matrix is a well-known phenomenon when barriers for conformational isomerization are low, as in the present case for the **T2b** → **T2a** transformation. Further, this effect has been shown to be especially significant when xenon is used as substrate. Moreover, it was also demonstrated that using a higher temperature of the substrate during deposition leads to a more extensive conformational cooling than that achieved by annealing up to the same temperature a matrix previously deposited at a lower temperature.[55] Hence, in the present case, a substrate temperature of 30 K during deposition is enough to achieve the same effects obtained by annealing up to 36 K the matrix deposited at 15 K, in particular the loss of **T2b**.

Argon Matrices Deposited at 15 K. The spectrum of the as-deposited **T**/Ar matrix at 15 K (middle trace in Figure 6) shows

Table 2. Experimental and B3LYP/6-311++G(2d,2p) Calculated (Scaled) Frequencies and Intensities of the Observed Photoproducts of T in Xenon and Argon Matrices

Calculated		Observed frequency				Approximate Description[a]
		Xe/Hg lamp		Laser		
ν	I	Xe (30 K)	Ar (13 K)	Xe (30 K)	Ar (15 K)	
1H-1,2,4-triazol-5-yl carbodiimide (P1)						
3463	101	3468, **3465**	3489, 3487	3468, **3465**	3489,3487	νNH(R)
3413	135	**3405**, 3401	3436	3405, 3400	3436	νNH(I')
3082	3	n.o.	n.o.	n.o.	n.o.	νCH
2185	1256	**2163**, 2138	**2171**, 2145	**2163**, 2138	**2171**, 2145	νC=N(I), FR
		~1660	~1666	~1660	~1663	overtone 2 δNH(I)
1570	200	1575, **1571**	1575, 1574	1575, **1571**	1575, 1573	νN1'-C5 + δ_{ring} + δN1'C5N4 + ν_{ring} + δNH(R)
1486	84	1495, 1482	1488	1496, 1483	1488	ν_{ring} + δ_{ring} + δN1'C5N4 + δCH
1406	11	1400	1402, 1401	1401, 1399	1402, 1401	δNH(R) + ν_{ring}
1334	23	1333	1336	**1333**, 1331	1336	ν_{ring}
1282	38	**1274**, 1271	1272	**1274**, 1271	1272	δCH + δ_{ring} + ν_{ring} + δN1'C5N4
1226	23	1222	1220	**1222**, 1220	1220	δNH(R) + ν_{ring} + δ_{ring} + δN1'C5N4
1181	4	1182	1187	1182	1187	ν_{ring}
1095	21	1080	1080	1080	1080	ν_{ring} + δ_{ring} + δN1'C5N4
1023	37	1022	1024, 1023, 1021, 1020	1022	1024, 1023, 1021, 1020	δ_{ring} + δN1'C5N4
963	10	**960**, 958	960	**960**, 959	960	δ_{ring} + δCH
890	12	882	886	883	886	γCH
850	427	789	**795**, 789	789	795	δNH(I) + τC5N1'C5'N4'
744	28	755	761	756	760	τC5N1'C5'N4' + γNH(I)
736	13	749, **745**	754, 753, 751	750, **745**	754, 753, 751	τC5N1'C5'N4' + τ_{ring} + γNH(I) + γN4N1N1'C5
681	42	676, **675**	**678**, 677	676, **675**	678, 677	τ_{ring}
562	49	542	536	542	536	τC5N1'C5'N4' + γNH(I)
540	6	531, **529**	529	531, **529**	529	τC5N1'C5'N4'
519	72	n.o.	n.o.	n.o.	n.o.	γNH(R) + δNH(I) + τC5N1'C5'N4' + τ_{ring}
1H-1,2,4-triazol-3-yl carbodiimide (P2)						
3465	109	3470, 3468	3507	3470, 3468	3507	νNH(R)
3407	104	3400, 3398, 3397	3430, **3426**, 3424	3400, 3397	3426	νNH(I)
3077	1	n.o.	n.o.	n.o.	n.o.	νCH
2184	1250	2160, 2144	2168, 2166, 2150, **2148**	2160, 2144	2164, 2150, **2148**	νC=N(I), FR
		~1660	~1666	~1660	~1663	overtone 2 δNH(I)
1545	273	1543	1548	1543	1548	ν_{ring} + νN1'-C5 + δ_{ring}
1497	7	n.o.	n.o.	n.o.	n.o.	ν_{ring} + δNH(R) + νN1'-C5
1448	22	1445	1443	1445	1443	ν_{ring} + δNH(R) + δ_{ring} + δCH
1334	13	1337	1335, 1334	1337, 1333, 1331	1335, 1334	ν_{ring} + νN=C(I) + δ_{ring}
1290	36	1284	1281	1284	1281	ν_{ring} + δ_{ring} + δCH
1239	55	**1234**, 1232	1236	1234	1236	ν_{ring} + νN=C(I) + δ_{ring} + δCH
1142	16	1148, 1145	1149	1148, 1144	1148	ν_{ring} + δNH(R)
1079	36	1062	1050, **1048**	1062	1048	ν_{ring} + δ_{ring} + δCH
980	5	982	n.o.	982	n.o.	δ_{ring} + δCH
980	5	982	n.o.	982	n.o.	δ_{ring} + δCH + ν_{ring}
880	396	817, 815, 813	**823**, 822	817, 815, 813	**823**, 822	δNH(I) + τC5N1'C5'N4'
844	17	853	855, 853, 851	853	855, 853, 851	γCH + τ_{ring}
761	14	751, 750	780	745	779	τ_{ring} + γN1'N1N4C5
733	19	740	747	740	747	τC5N1'C5'N4'
662	6	662	n.o.	662	n.o.	τ_{ring}
560	46	543	533, 532	543, 542, 541	534, 532	τC5N1'C5'N4' + γNH(I)
546	9	535	n.o.	535	n.o.	τC5N1'C5'N4'
504	81	n.o.	n.o.	n.o.	n.o.	γNH(R) + τ_{ring}

[a] Abbreviations: ν, bond stretching; δ, bending, deformation in plane; γ, out-of-plane bending; τ; torsion, FR, Fermi resonance; R, triazole ring; I, carbodiimide moiety.

the same characteristic bands originating from the three most stable **T** species as observed for the xenon matrix deposited at 15 K. However, since the multiple site splitting of some bands observed in the **T**/Xe spectrum did not appear in solid argon, the **T**/Ar spectrum fits even better the sum spectrum calculated for three **T1**, **T2a**, and **T2b** species.

Positions of the bands observed for **T1**, **T2a**, and **T2b** in xenon and argon matrices together with the frequencies predicted by calculations are given in Table S2 in the Supporting Information. The assignment of these bands is based on the analysis of the theoretical spectra and the potential energy distribution (PED) matrices.
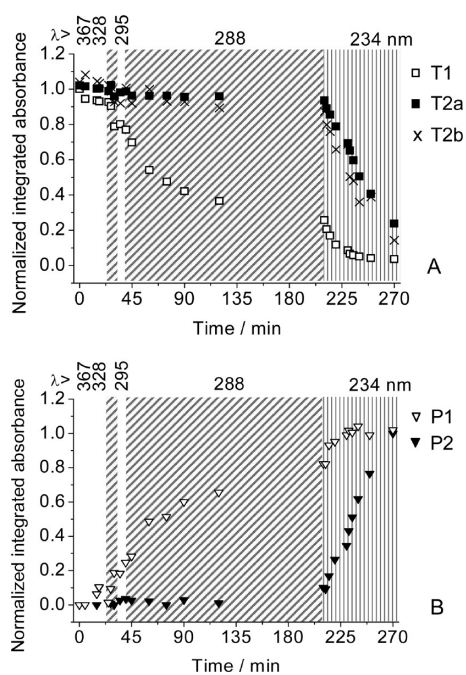
Figure 9. Plots of the normalized integrated absorbance versus irradiation time observed for bands in the **T**/Ar spectra at 13 K after broadband photolysis with the high-pressure Xe/Hg lamp: open squares, the **T1** band at ca. 1595 cm^{-1}; solid squares, the **T2a** band at ca. 1580 cm^{-1}; crosses, the **T2b** band at 1523 cm^{-1}; open triangles, the P1 band at ca.789 cm^{-1}; solid triangles, the P2 band at ca. 820 cm^{-1}. Normalization of the integrated absorbance was performed relative to the most intense band in the given series. Different hatch corresponds to the different UV-irradiation conditions, which are specified at the top of each frame.

It is generally accepted that xenon is a better matrix gas to induce conformational cooling than argon. It means that in the spectra of xenon matrices one should expect the higher **T2a**/**T2b** population ratio as compared with the argon experiment performed at the same temperature. Indeed, the **T2a**/**T2b** values estimated from the spectra of freshly deposited xenon and argon matrices at 15 K are equal to 2.64 and 1.32, respectively.

■ RESULTS OF THE UV IRRADIATION EXPERIMENTS

High Pressure Xe/Hg Lamp. *T in Xenon Matrix Deposited at 30 K.* UV irradiation (λ >288 nm) of the **T**/Xe matrix deposited at 30 K (only the two most stable **T** forms present), using a high-pressure Xe/Hg lamp, led to fast consumption of tautomer **T1**, as shown by rapid reduction (ca. 50% in 5 min) of the intensity of the bands assigned to this species, while **T2a** remained intact. An almost complete depletion of **T1** was observed after 30 min of irradiation. Simultaneously, new bands appeared, which must be due to a photochemical product (**P1**). Upon subsequent irradiation of the matrix with UV light of shorter wavelengths (λ >234 nm), the set of bands due to the **T2a** tautomer strongly decreased during 25 min of photolysis. At the same time, a set of bands showed up in the spectra, which are due to a second photoproduct (**P2**). The results are summarized in Figure 8, where representative regions of the **T**/Xe difference spectra before and after photolysis are shown together with the corresponding difference spectra calculated for the **T1** and **T2a** tautomers and the suggested photoproducts, **P1** and **P2**, whose structure will be revealed later on in this paper. The most
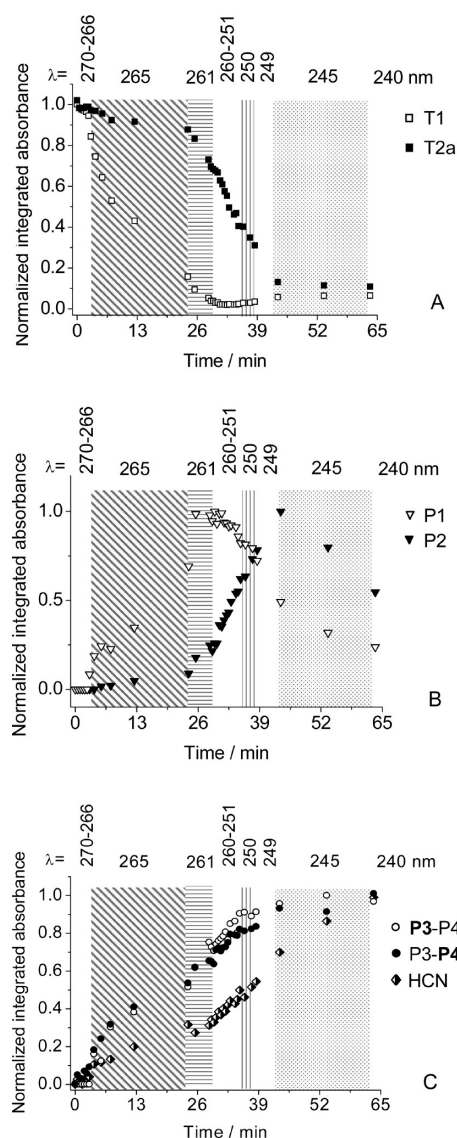

Figure 10. Plots of the normalized integrated absorbance vs irradiation time observed for the selected bands in the **T**/Ar spectra at 15 K after photolysis with laser: open squares, the **T1** band at ca. 1595 cm^{-1}; solid squares, the **T2a** band at ca. 1580 cm^{-1}; open triangles, the P1 band at ca. 789 cm^{-1}; solid triangles, the P2 band at ca. 820 cm^{-1}; open circles, **P3**−P4 band at ca. 2300 cm^{-1}; solid circles, **P3**−**P4** band at ca. 2054 cm^{-1}; half-solid rhombs, HCN broad absorption between 3310 and 3265 cm^{-1}. Normalization of the integrated absorbance was performed relative to the most intense band in the given series. Different hatch corresponds to the different UV-irradiation conditions, which are specified at the top of each frame.

prominent features of the photoproducts were observed in the 3500−3350 and 2200−2100 cm^{-1} spectral regions. Other new bands could also be observed below 1600 cm^{-1}, including several intense features at 1571, 1543, 816, 789, and 675 cm^{-1}. Similarly as for the precursors, many bands in the spectra of the photolyzed matrix appeared split due to existence of different matrix sites (especially in the ν(NH) stretching region). The complete list of bands arising from the photolysis of **T**/Xe deposited at 30 K is presented in Table 2.

T in Argon Matrix Deposited at 13 K. As already mentioned, when **T** was deposited in argon at 13 K three **T** species (**T1**, **T2a**, and
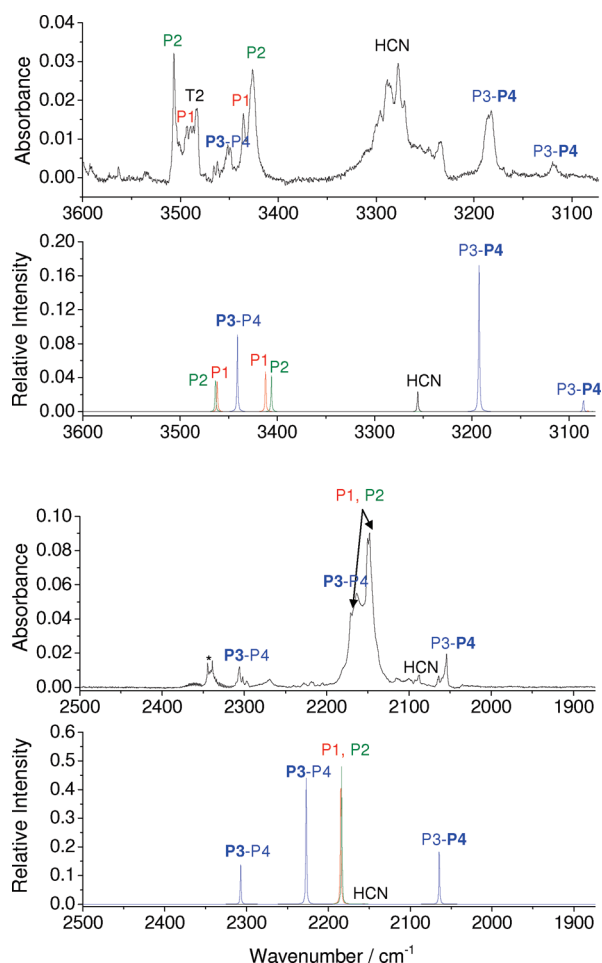
Figure 11. Selected regions of the spectra: experimental spectrum of **T** isolated in argon matrix at 15 K after laser irradiation (upper trace) and theoretical spectra of **P1**, **P2**, **P3**−**P4**, and HCN (lower traces).

T2b) were present in the matrix. As it can be noticed from Table 2, broad band irradiations (λ >288 nm and λ >234 nm) applied to **T** isolated in argon led to the appearance of sets of bands corresponding to the same photoproducts as observed in xenon matrices.

Figure 9 presents plots of the normalized integrated absorbance changes of selected bands of **T1**, **T2a**, and **T2b** and of their photoproducts observed in an argon matrix deposited at 13 K versus the photolysis time with different UV filters. The analysis of these plots indicates that upon irradiation using the λ >288 nm filter a gradual decrease of the T1 bands (open squares) is observed, with simultaneous growth of the absorptions due to P1 photoproduct (open triangles). When shorter wavelengths are applied (λ >234 nm), a quick decrease of the **T2a** (solid squares) and **T2b** bands (crosses) is observed together with the appearance and strong increase of the **P2** photoproduct bands (solid triangles).

Irradiation Using Narrow Band Tunable UV Light. A series of irradiations of xenon (30 K) and argon (15 K) matrix-isolated **T** was carried out with narrow band radiation in the 290−240 nm range, with different wavelength steps ranging from 10 to 1 nm.

Figure 10 shows the normalized integrated absorbance changes of the selected precursor and products bands observed for the **T**/Ar matrices versus the photolysis time with the different laser wavelengths used. The onset of the **T** destruction in solid argon starts already at 270 nm. However, a quick decrease

of its bands is observed at 265 nm. After 5 min of irradiation at the latter wavelength, ca. 50% of the intensity of the bands due to **T1** vanishes. The photolysis of **T1** proceeds further when shorter wavelengths are applied (264−260 nm). On the other hand, radiation of $\lambda \geq 265$ nm does not cause apparent changes in the population of **T2a** in an argon matrix, and the photodecomposition of this species starts only at shorter laser wavelength (261 nm). A similar course of the photolysis process was observed when the laser irradiation of the **T**/Xe matrix was performed. The analysis of the plots presented in Figure 10 indicates that a maximum of the photoproducts concentration coincides with the regions where the precursors bands decline. On further photolysis, the intensities of the bands due to the products start to decrease, indicating the occurrence of additional photochemical reactions. We shall turn to this point later on in this paper.

Comparison of the laser irradiation results with those reported for the Xe/Hg lamp experiments revealed that, although appearing in a much shorter time scale, the main observed photoproducts are the same. However, laser irradiation led to the appearance in both Ar and Xe matrices of additional new bands that were not present when the broad band irradiation source was used. Figure 10C shows a plot of the normalized integrated absorbance versus photolysis time at different laser wavelengths for three of the absorptions appearing exclusively when laser irradiation was performed. The profiles of variation strongly differ from those obtained for **P1** and **P2** products, and indicate that the additional photoproducts appearing during laser irradiation of the **T** isolated in Ar, as well as in Xe matrices, correspond to secondary photoproducts formed from **P1** and **P2**. The structures of these secondary products will be discussed later on in this paper. Figure 11 shows two representative regions of the spectra of **T**/Ar (15 K) matrices, indicating the presence, besides the **P1** and **P2** bands, of the additional bands resulting from the UV irradiation with the laser source. The positions of all additional features appearing in the spectra during the laser irradiation are collected in Table 3, together with their suggested assignments.

Tautomer-Selective Photochemistry. In the course of the performed photolysis experiments an interesting phenomenon was detected concerning different threshold energies necessary to start the photolysis of **T1** and **T2a** (**T2b**). Such tautomer selectivity was observed both for Xe lamp irradiation with the UV optical filters, as it is seen from Figure 8, and for the narrow-band source, as shown in Figure 12, where several regions of the infrared spectra of the laser irradiated **T**/Ar matrix are presented. This highly tautomer-specific photochemistry is also very well evident in Figures 9 and 11. The UV irradiation with the λ >288 nm filter or the laser irradiation with 265 nm wavelength led almost exclusively to the consumption of the **T1** tautomer, while a subsequent irradiation using shorter wavelengths (λ >234 nm) or irradiation of the matrix with shorter laser wavelengths (λ = 261 nm) was necessary for the **T2a** (**T2b**) tautomer destruction. It is worth noting that, taking into account the transmittance characteristics of the optical filters used (see Matrix Isolation Studies in Experimental and Computational Methods), there is no contradiction in the values of the threshold energies in the Xe lamp and laser irradiation experiments. The observed phenomenon of the tautomer-selective photochemistry of **T** can be understood in light of the results of the performed time-dependent density functional theory (TD-DFT) calculations. Indeed, the estimated LUMO−HOMO energy gap for **T1** differs apparently from that calculated for the **T2a** and **T2b** tautomers, being equal to 235.1, 217.7, and 218.8 nm for **T1**,

Table 3. Comparison of the Frequencies (cm^{-1}) and Intensities ($km\ mol^{-1}$) Calculated for the Selected Photoproducts Associates and Observed in the Laser Irradiated T/Ar Matrices

calculated				observed frequency			
ν	I	ν	I	Ar (15 K)	reference	approximate description[a]	subunit
HCN		HCN−N_2					
3257	67	3239	144	3278	3304[b]	ν(CH)	HCN
		2401	0	n.o.		ν(N≡N)	N_2
2158	1	2156	7	2088	2093[b]	ν(N≡C)	HCN
739	39	772	38	734, 733	720[b]	γ(CH)	HCN
739	39	767	30	734, 733	720[b]	δ(CH)	HCN
HNC		HNC−N_2					
3600	263	3541	608	3600	3620[c]	ν(NH)	HNC
		2404	1	n.o.		ν(N≡N)	N_2
2064	72	2066	50	2064	2029[c]	ν(N≡C)	HNC
405	140	503	132	n.o.		γ(NH)	HNC
405	140	496	113	n.o.		δ(NH)	HNC
P3−P4		**P3−P4**−N_2					
3442	232	3404	632	3450		ν(NH)	**P3**
3194	503	3189	534	3184	3250.1[d]	ν(NH)	**P4**
3086	39	3085	39	3119	3142.5[d]	ν(CH)	**P4**
		2403	1	n.o.		ν(N≡N)	N_2
2308	351	2306	374	2306, 2302, 2297		ν_{as}(NCN)	**P3**
2228	1232	2231	1296	2163		ν_{as}(NCN)	**P3**
2065	551	2064	551	2054	2032.7[d]	ν_{as}(NNC)	**P4**
1435	17	1435	29	n.o.		ν_s(NCN)	**P3**
1340	117	1341	118	1329	1278.1[d]	δ(NH)	**P4**
1239	67	1239	65	1231	1187.5[d]	ν_s(NNC) + δ(NH)	**P4**
893	41	896	42	792	792.1[d]	γ(NH) + γ(CH)	**P4**
884	8	886	7	n.o.		ν_s(CNC) + δ(CNC) + δ(NCN)	**P3**
770	414	782	460	n.o.		δ(NH) + δ(NCN)	**P3**
689	389	693	389	675	606.5[d]	δ(CH) + δ(CNN)	**P4**
615	9	624	3	n.o.		δ(CNC) + δ(NCN)	**P3**
564	52	590	66	n.o.		γ(NH) + δ(CNC) + δ(NCN)	**P3**
526	75	527	72	n.o.	461.4[d]	δ(CH) + δ(CNN)	**P4**

[a] Abbreviations: ν, bond stretching; δ, bending, deformation in plane; γ, out-of-plane bending. [b] Reference 60. [c] Reference 61. [d] Reference 25.

T2a, and **T2b**, respectively. The corresponding electronic transitions are predicted to be characterized by relatively high oscillator strengths: 0.2766 (**T1**), 0.2650 (**T2a**), and 0.2381 (**T2b**).

Identification of the Photoproducts. *Main Products Appearing in Both Broad Band and Laser Irradiation Experiments.* In order to identify the photoproducts formed from the **T** molecule, a number of different putative structures was optimized and their IR spectra calculated at the B3LYP/6-311++G-(2d,2p) level. The interpretation of the experimental data was based on both the DFT calculations and previously reported infrared spectra of possible photoproducts or their analogues, whenever available.

The main photochemistry pathways resulting from irradiation of the **T1**, **T2a**, and **T2b** species in the studied matrices are schematically shown in Figure 13.

A comparison of the positions and intensities of the new bands appearing after photolysis with those calculated for the possible photoproducts shows that the N_2 elimination pathway and formation of carbodiimide is the dominating route of the **T** photolysis, both in xenon and in argon matrices. Further inspection of the spectra of the matrices after irradiation shows

that both **T1** and **T2a** tautomers photolyze according to the same pathway, yielding analogous products differing in the position of the H-atom attached to the triazole ring, 1*H*-1,2,4-triazol-5-yl carbodiimide (**P1**) and 1*H*-1,2,4-triazol-3-yl carbodiimide (**P2**). The set of bands appearing first in the spectra, at the expense of **T1**, when lower energy radiation was applied (broad band photolysis with λ >288 nm or monochromatic radiation at λ = ca. 265 nm), fits nicely the calculated spectrum of the 1*H*-1,2,4-triazol-5-yl carbodiimide (**P1**). In turn, the group of bands appearing at the expense of **T2**, when higher energy radiation was applied (broad band photolysis with λ >234 nm or monochromatic radiation at λ = ca. 245 nm) fits very well the 1*H*-1,2,4-triazol-5-yl carbodiimide (**P2**) spectrum. The presence of the third precursor molecule (**T2b**) in the matrices deposited at 15 K did not give rise to any additional features observed in the spectra after irradiation, indicating that, as shown in Figure 13, the photolysis of **T2a** and **T2b** leads to the same photoproducts.

According to the B3LYP/6-311++G(2d,2p) calculations, the N−N bonds that undergo cleavage in the observed photoreactions are the tetrazole weakest, formally single bonds. which are
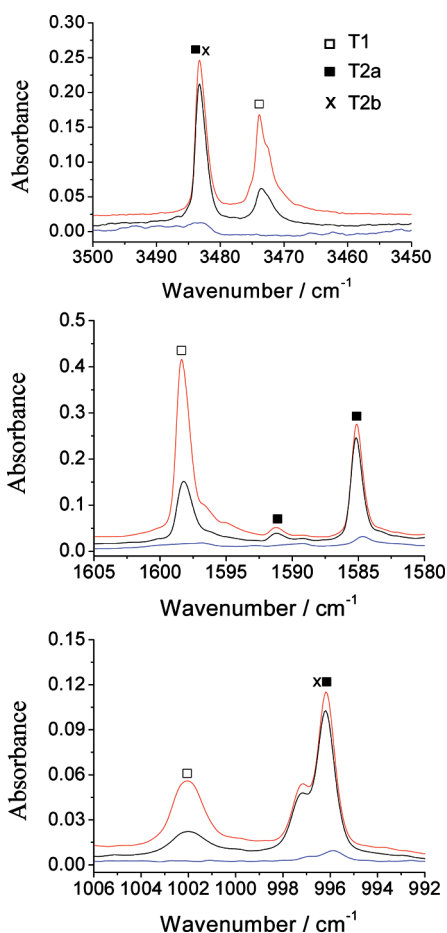
5703

dx.doi.org/10.1021/jp202925r |*J. Phys. Chem. A* 2011, 115, 5693–5707

Figure 12. Tautomer-selectivity in representative regions of the spectra of the **T**/Ar matrix: directly after deposition at 15 K (red line), after laser irradiation with $\lambda = 265$ nm (black line); after laser irradiation with $\lambda = 263-245$ nm (blue line).

Figure 13. Proposed pathways for the main photochemistry resulting from irradiation of the **T**/Ar and **T**/Xe matrices. The calculated ZPE corrected ground-state reaction energies are given in kJ mol^{-1}.

longer than 1.360 Å. The formation of the **P1** and **P2** products proceeds most probably through the 1-(1*H*-1,2,4-triazol-5-yl)-diaziridene and 1-(1*H*-1,2,4-triazol-3-yl)diaziridene intermediates (see Figure 13). However, these species seem to be unstable and were not detected experimentally.

The most intense bands of **P1** and **P2** were found in 3500−3380 cm^{-1} spectral region, characteristic of the stretching modes of the N−H groups, and 2200−2100 cm^{-1}, due to the antisymmetric stretching mode of the N═C═N(H) carbodiimide moiety. Intense bands were also observed between 1590 and 1540 cm^{-1} and 830−780 cm^{-1}, originating from the N−H bending modes. It is visible in Figure 8 that in the N−H stretching region both **P1** and **P2** photoproducts in Xe matrices give rise to extensively site split bands, as observed for their precursor species (see Xenon Matrices Deposited at 15 K and Table S2 in the Supporting Information). In turn, the extra bands in the ν_{as}(N═C═N) region, between 2200 and 2100 cm^{-1}, found both in solid Xe and Ar, are most likely the overtone of the N—N stretching mode of the aromatic substituent in strong Fermi resonance with the antisymmetric stretching mode, ν_{as}(N═C═N). The ν(N—N) fundamental modes are situated at 1080 and 1048 cm^{-1} in the spectra of **P1** and **P2**, respectively, isolated in an argon matrix. The Fermi resonance doublets for carbodiimides with aromatic substituents are well-known.[56]
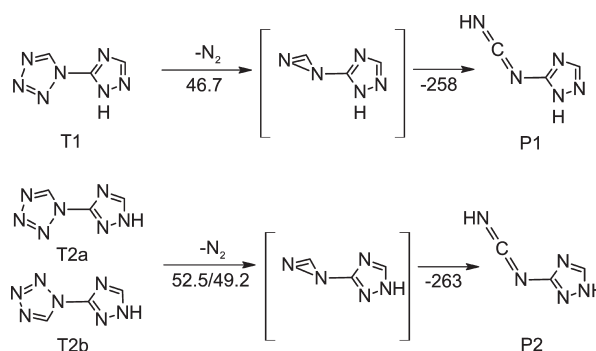
The observed preference for the reaction path leading to the carbodiimide plus N$_2$ is in agreement with the calculated ground-state reaction energies, which are also provided in Figure 13. The obtained result was not unexpected, since it has been shown that 1,5-disubstituted tetrazoles were useful precursors of carbodiimides (R—N═C═N—R′), while 1-substituted tetrazoles give rise to monosubstituted carbodiimides R—N═C═N—H. The latter molecules were found to be stable at low temperatures but izomerize to cyanamides RNH—CN at ordinary temperatures.[57] The simplest unsubstituted carbodimide, HN═C═NH, was for the first time obtained and spectroscopically characterized in argon matrices after cyanamide pyrolysis.[58] Later on, Maier et al.[25] identified this molecule as one of the products detected after tetrazole photolysis in solid argon. Recently, Gómez-Zavaglia et al.[30] have shown that in situ UV irradiation ($\lambda > 235$ nm) of matrix isolated 5-mercapto-1-methyltetrazole may lead to simultaneous elimination of molecular nitrogen and sulfur with production of *N*-methylcarbodiimide. To the best of our knowledge, neither 1*H*-1,2,4-triazol-5-yl carbodiimide (**P1**) nor 1*H*-1,2,4-triazol-3-yl carbodiimide (**P2**) molecules have ever been described before.

Both **P1** and **P2** photoproducts are expected to exist in two conformers (denoted as **P1**, **P1a**, and **P2**, **P2a**, see Figure 14), originating from the different positions of the HNCN moiety relative to the triazole ring. Only the most stable species from each pair (**P1** and **P2**), characterized by the trans position of the HNCN substituent with respect to the NH group of the triazole ring, was detected experimentally in the studied matrices. If all four **P1**, **P1a**, **P2**, and **P2a** species are produced in the photochemical process, then the higher energy conformers (**P1a**, **P2a**) must quickly isomerize to their more stable counterparts (**P1**, **P2**). This observation agrees with the calculated energy difference, ΔE_{ZPE}, in the (**P1**, **P1a**) and (**P2**, **P2a**) pairs of conformers of 14.2 and 3.20 kJ mol^{-1}. It is also in agreement with the low calculated energy barriers for **P1a** → **P1** and **P2a** → **P2** isomerizations, which amount to 2.80 and 9.06 kJ mol^{-1}, respectively.

It is worth mentioning that, besides the different onsets observed for decomposition of **T1** and **T2**, there are no cross-transformations detected in the studied matrices. After **T1** is consumed to form **P1**, the only remaining substrate is **T2**. When **T2** consumption starts, there is no tautomerization from **T2** to **T1**, since no repopulation of bands due to **T1** is observed. Moreover, the secondary product **P2**, produced from **T2**, has a different spectral signature, comparing to **P1** (produced from **T1**). This confirms the absence of proton shift both in substrate
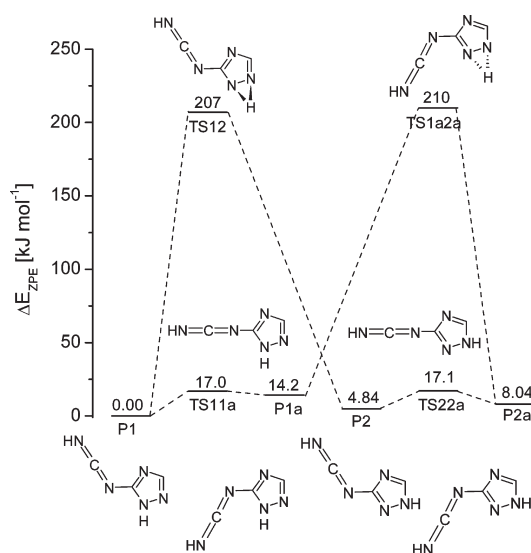
5704

dx.doi.org/10.1021/jp202925r |*J. Phys. Chem. A* 2011, 115, 5693–5707

Figure 14. B3LYP/6-311++G(2d,2p) ZPE corrected potential energy diagram for the **P1** and **P2** conformers.

Figure 15. Proposed pathways for the minor photochemistry resulting from irradiation of the **T**/Ar and **T**/Xe matrices using narrow-band source.

(**T1** and **T2**) and in the products (**P1** and **P2**) under the present experimental conditions. The lack of the **P1** ↔ **P2** interconversion is justified by the high energy barriers calculated for this process (see Figure 14).

Minor Products Appearing in Laser Irradiation Experiments. As mentioned earlier (see Irradiation Using Narrow Band Tunable UV Light) several additional bands appeared in the spectra of **T**/Ar and **T**/Xe matrices when the laser irradiation was applied. In an attempt to elucidate the structures of the photoproducts that give rise to these absorptions, several possible rearrangements within the carbodiimide moiety in the **P1** and **P2** products were examined. The respective structures and infrared spectra, calculated at B3LYP/6-311++G(2d,2p) level, are shown in the Supporting Information (Table S3). None of these species allowed for a satisfactory reproduction of the observed experimental frequencies. In the next step, a number of decomposition pathways available for both the precursors and the **P1** and **P2** photoproducts, together with additional possible rearrangements of the newly formed species, were considered.

The proposed photolysis pathways in the laser irradiation experiments, leading to minor products, are presented in Figure 15. On the basis of the performed calculations, two other species, in addition to **P1** and **P2** products, may be present in the photolyzed matrices, namely, *N*-cyanocarbodiimide HNCNCN (**P3**) and nitrilimine HNNCH (**P4**). To the best of our knowledge, **P3** has not been described in the literature until now, although its isomer diazoacetonitrile NNCHCN is known.[59] On the other hand, nitrilimine **P4** has been previously identified in low temperature matrices by Maier et al.[25] Both species (**P3**, **P4**), are expected to interact with each other or/and with N_2 formed in the same matrix cage and to form molecular complexes. Table 3 presents the positions of the observed bands of those **P3**–**P4** and **P3**–**P4**–N_2 complexes for which the best fit was observed between calculated and experimental frequencies.

The observed kinetics for the main photoproducts **P1** and **P2** suggests that some of these molecules are split on laser irradiation into small fragments. This process probably proceeds through
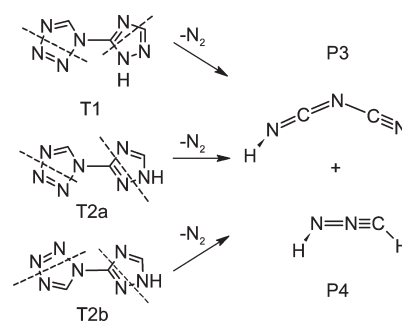
different unstable intermediates and their structure under the conditions of the experiment is impossible to explore. The main of these small products is HCN, which gives rise to three fundamental bands. For monomeric HCN in solid argon, the most intense of these bands, due to the ν(CH) stretching mode, is expected at ca. 3304 cm^{-1}.[60] Absorptions observed in the 3350−3150 cm^{-1} range in the spectra of the irradiated matrices obtained in the present study differ from those appearing in the spectra of the HCN monomer. However, both in Ar and Xe matrices a broad structured absorption is observed with global maximum at 3277 cm^{-1} that is consistent with the presence of HCN complexed with other species formed in the same matrix cage during the studied photodecomposition processes. On the other hand, the appearance of weak bands at 3600 and 2064 cm^{-1} indicates the presence of HNC in the photolyzed matrices. The weakness of these bands suggests that the HNC → HCN isomerization[61] takes place in the studied matrices as well.

■ CONCLUSIONS

The three most stable forms of the 5-(1*H*-tetrazol-1-yl)-1,2,4-triazole molecule (**T1**, **T2a**, and **T2b**) according to the B3LYP/6-311++G(2d,2p) predictions were identified in argon and xenon matrices deposited at 15 K. The global minimum is **T1**, which possesses the annular H7 atom attached to the N1 atom of the triazole ring. Tautomer **T2a** has a slightly higher energy (ΔE_{ZPE} = 3.65 kJ mol^{-1}) and has its triazole ring H-atom at N2 position. The third observed species, **T2b** (ΔE_{ZPE} = 6.92 kJ mol^{-1}), being the same prototropic tautomer form as **T2a**, is characterized by different mutual arrangement of the triazole and tetrazole rings. The observation of all three **T1**, **T2a**, and **T2b** species in the studied matrices is in contradiction with the calculated high value for the energy barrier between **T1** and **T2a** tautomers of 212 kJ mol^{-1}. An explanation for the observed coexistence of **T1**, **T2a**, and **T2b** is a significant lowering of the **T1** ↔ **T2a** energy barrier in the **T** dimer structures (that are likely to be the building blocks in the crystalline phase) as compared to the unimolecular tautomerization. Both deposition of the matrices at higher temperatures and their annealing result in the presence of only the two most stable **T1** and **T2a** forms. Indeed, due to the **T2b** → **T2a** conversion, these samples are devoid of **T2b**, in agreement with the predicted low energy barrier for this transformation (5.38 kJ mol^{-1}).

Broad band irradiation of the **T**/Ar and **T**/Xe matrices led to observation of one main photochemical process, occurring consecutively for **T1** (λ > 288 nm) and **T2a** and **T2b** (λ > 234 nm).

This pathway involves cleavage of the tetrazole ring of the precursor molecules, the N_2 molecule elimination, and formation of the corresponding carbodiimide. The 1H-1,2,4-triazol-5-yl carbodiimide (**P1**) and 1H-1,2,4-triazol-3-yl carbodiimide (**P2**), differing by the position of the annular H-atom attached to the triazole ring, are then formed as a result of the unimolecular decomposition of **T1** and **T2a** (and **T2b**), respectively.

When narrow band irradiation is used in the photolysis, the same **P1** and **P2** species appeared as dominating photoproducts. In addition, several other species, originating from decomposition of the main products **P1** and **P2**, were identified in the spectra of the matrices irradiated with the laser, in particular, N-cyanocarbodiimide HNCNCN (**P3**) hydrogen bonded to nitrilimine HNNCH (**P4**) and HCN molecules.

The main observed pathway of the unimolecular decomposition of **T** isomers to form **P1** and **P2** products appeared to be a highly tautomer-specific photoreaction. The UV irradiation with the λ >288 nm filter or the laser irradiation with 265 nm wavelength led almost exclusively to the consumption of the **T1** tautomer, while a subsequent irradiation using shorter wavelengths (λ >234 nm) or irradiation of the matrix with the shorter laser wavelengths was necessary for the **T2a** (**T2b**) tautomer destruction.

■ ASSOCIATED CONTENT

ⓢ **Supporting Information.** Selected geometric parameters calculated at B3LYP/6-311++G(2d,2p) level for **T1**, **T2a**, **T2b**, and **T4** (Table S1), experimental and calculated frequencies and intensities for **T1**, **T2a**, and **T2b** in xenon and argon matrices (Table S2), and structures and infrared spectra of putative photoproducts calculated at B3LYP/6-311++G-(2d,2p) level (Table S3). This material is available free of charge via the Internet at http://pubs.acs.org.

■ ACKNOWLEDGMENT

■ REFERENCES

(1) Herr, R. J. *Bioorg. Med. Chem.* **2002**, *10*, 3379–3393.

(2) May, B. C. H.; Abell, A. D. *J. Chem. Soc., Perkin Trans.* **2002**, *1*, 172–178.

(3) Bekircan, O.; Bektas, H. *Molecules* **2006**, *11*, 469–477.

(4) Myznikov, L. V.; Hrabalek, A.; Koldobskii, G. I. *Chem. Heterocycl. Compd.* **2007**, *43*, 1–9.

(5) Rostom, S. A. F.; Ashour, H. M. A.; Abd El Razik, H. A.; Abd El Fattah, H.; El-Din, N. N. *Bioorg. Med. Chem.* **2009**, *17*, 2410–2422.

(6) Galvez-Ruiz, J. C.; Holl, G.; Karaghiosoff, K.; Klapötke, T. M.; Lohnwitz, K.; Mayer, P.; Noth, H.; Polborn, K.; Rohbogner, C. J.; Suter, M.; Weigand, J. J. *Inorg. Chem.* **2005**, *44*, 4237–4253.

(7) Sivabalan, R.; Anniyappan, M.; Pawar, S. J.; Talawar, M. B.; Gore, G. M.; Venugopalan, S.; Gandhe, B. R. *J. Hazard. Mater.* **2006**, *137*, 672–680.

(8) Stierstorfer, J.; Tarantik, K. R.; Klapötke, T. *Chem.—Eur. J.* **2009**, *15*, 5775–5792.

(9) Klapötke, T.; Sabaté, C. M.; Rasp, M. *J. Mater. Chem.* **2009**, *19*, 2240–2252.

(10) Tao, G.-H.; Twamley, B.; Shreeve, J. M. *J. Mater. Chem.* **2009**, *19*, 5850–5854.

(11) Bronisz, R. *Inorg. Chem.* **2005**, *44*, 4463–4465.

(12) Liu, B.; Zhang, X.-C.; Wang, Y.-F. *Inorg. Chem. Commun.* **2007**, *10*, 199–203.

(13) Quesada, M.; Prins, F.; Roubeau, O.; Gamez, P.; Teat, S. J.; van Koningsrruggen, P. J.; Haasnoot, J. G.; Reedijk, J. *Inorg. Chim. Acta* **2007**, *360*, 3787–3796.

(14) Białońska, A.; Bronisz, R.; Weselski, M. *Inorg. Chem.* **2008**, *47*, 4436–4465.

(15) Krivokapic, I.; Enachescu, C.; Bronisz, R.; Hauser, A. *Chem. Phys. Lett.* **2008**, *455*, 192–196.

(16) Yu, J.-H.; Mereiter, K.; Hassan, N.; Feldgitscher, C.; Linert, W. *Cryst. Growth Des.* **2008**, *8*, 1535–1540.

(17) Liu, P.-P.; Cheng, A.-L.; Yue, Q.; Liu, N.; Sun, W.-W.; Gao, E.-Q. *Cryst. Growth Des.* **2008**, *8*, 1668–1674.

(18) Sorescu, D. C.; Bennett, C. M.; Thompson, D. L. *J. Phys. Chem. A* **1998**, *102*, 10348–10357.

(19) Abboud, J-L. M.; Foces-Foces, C.; Notario, R.; Trifonov, R. E.; Volovodenko, A. P.; Ostrovskii, V. A.; Alkorta, I.; Elguero, J. *Eur. J. Org. Chem.* **2001**, *16*, 3013–3024.

(20) Bugalho, S. C. S.; Maçôas, E. M. S.; Cristiano, M. L. S.; Fausto, R. *Phys. Chem. Chem. Phys.* **2001**, *3*, 3541–3547.

(21) Palmer, M. H.; Christem, D. *J. Mol. Struct.* **2004**, *705*, 177–187.

(22) Frija, L.; Reva, I. D.; Gómez-Zavaglia, A.; Cristiano, M. L.; Fausto, R. *J. Phys. Chem. A* **2007**, *111*, 2879–2888.

(23) Pagacz-Kostrzewa, M.; Bronisz, R.; Wierzejewska, M. *Chem. Phys. Lett.* **2009**, *473*, 238–246.

(24) Pagacz-Kostrzewa, M.; Bialonska, A.; Bronisz, R.; Wierzejewska, M. *J. Mol. Struct.* **2010**, *976*, 431–439.

(25) Maier, G.; Eckert, J.; Bothur, A.; Reisenauer, H. P.; Schmidt, C. *Liebigs Ann.* **1996**, 1041–1053.

(26) Kiszka, M.; Dunkin, I. R.; Gębicki, J.; Wang, H.; Wirz, J. *J. Chem. Soc., Perkin Trans. 2* **2000**, *12*, 2420–2426.

(27) Gómez-Zavaglia, A.; Reva, I. D.; Frija, L.; Cristiano, M. L.; Fausto, R. *J. Photochem. Photobiol., A* **2006**, *179*, 243–255.

(28) Frija, L. M.; Khmelinskii, I. V.; Cristiano, M. L. S. *J. Org. Chem.* **2006**, *71*, 3583–3591.

(29) Gómez-Zavaglia, A.; Reva, I. D.; Frija, L.; Cristiano, M. L.; Fausto, R. *J. Photochem. Photobiol., A* **2006**, *180*, 175–183.

(30) Gómez-Zavaglia, A.; Reva, I. D.; Frija, L.; Cristiano, M. L.; Fausto, R. *J. Mol. Struct.* **2006**, *786*, 182–192.

(31) Evans, R. A.; Wah Wong, M.; Wentrup, C. *J. Am. Chem. Soc.* **1996**, *118*, 4009–4017.

(32) Vosswinkel, M.; Lüerssen, H.; Kvaskoff, D.; Wentrup, C. *J. Org. Chem.* **2009**, *74*, 1171–1178.

(33) Kvaskoff, D.; Bednarek, P.; Wentrup, C. *J. Org. Chem.* **2010**, *75*, 1600–1611.

(34) Frija, L. M.; Ismael, A.; Cristiano, M. L. S. *Molecules* **2010**, *15*, 3757–3774.

(35) The abbreviation **T** is used when the position of the annular triazole ring proton in the studied molecule is not specified.

(36) Aouial, P. M.; Viallefont, P.; Ammari, L. E. *Acta Crystallogr., Sect. C* **1991**, *47*, 1866–1868.

(37) Steel, P. J. *J. Chem. Crystallogr.* **1996**, *26*, 399–402.

(38) Frisch, M. J.; Trucks, G. W.; Schlegel, H. B.; Scuseria, G. E.; Robb, M. A.; Cheeseman, J. R.; Montgomery, J. A., Jr.; Vreven, T.; Kudin, K. N.; Burant, J. C.; Millam, J. M.; Iyengar, S. S.; Tomasi, J.; Barone, V.; Mennucci, B.; Cossi, M.; Scalmani, G.; Rega, N.; Petersson, G. A.; Nakatsuji, H.; Hada, M.; Ehara, M.; Toyota, K.; Fukuda, R.; Hasegawa, J.; Ishida, M.; Nakajima, T.; Honda, Y.; Kitao, O.; Nakai, H.; Klene, M.; Li, X.; Knox, J. E.; Hratchian, H. P.; Cross, J. B.; Bakken, V.; Adamo, C.; Jaramillo, J.; Gomperts, R.; Stratmann, R. E.; Yazyev, O.; Austin, A. J.; Cammi, R.; Pomelli, C.; Ochterski, J. W.; Ayala, P. Y.; Morokuma, K.; Voth, G. A.; Salvador, P.; Dannenberg, J. J.; Zakrzewski, V. G.; Dapprich, S.; Daniels, A. D.; Strain, M. C.; Farkas, O.; Malick, D. K.; Rabuck, A. D.; Raghavachari, K.; Foresman, J. B.; Ortiz, J. V.; Cui, Q.; Baboul, A. G.; Clifford, S.; Cioslowski, J.; Stefanov, B. B.; Liu, G.;

Liashenko, A.; Piskorz, P.; Komaromi, I.; Martin, R. L.; Fox, D. J.; Keith, T.; Al-Laham, M. A.; Peng, C. Y.; Nanayakkara, A.; Challacombe, M.; Gill, P. M. W.; Johnson, B.; Chen, W.; Wong, M. W.; Gonzalez, C.; Pople, J. A. *Gaussian 03*; Gaussian, Inc.: Wallingford, CT, 2004.

(39) Martin, J. M. L.; Van Alsenoy, C. *GAR2PED*; University of Antwerp: Antwerpen, Belgium, 1995.

(40) Irikura, K. National Institute of Standards and Technology: Gaithesburg, MD, 1995.

(41) Cossi, M.; Scalmani, G.; Rega, N.; Barone, V. *J. Chem. Phys.* **2002**, *117*, 43–54.

(42) Cossi, M.; Rega, N.; Scalmani, G.; Barone, V. *J. Comput. Chem.* **2003**, *24*, 669–681.

(43) Bauernschmitt, R.; Ahlrichs, R. *Chem. Phys. Lett.* **1996**, *256*, 454–464.

(44) Stratmann, R. E.; Scuseria, G. E.; Frisch, M. *J. Chem. Phys.* **1998**, *109*, 8218–8224.

(45) Claramunt, R. M.; López, C.; García, M. A.; Otero, M. D.; Torres, M. R.; Pinilla, E.; Alarcón, S. H.; Alkorta, I.; Elguero, J. *New J. Chem.* **2001**, *25*, 1061–1068.

(46) Klapötke, T. M.; Sabaté, C. M.; Stierstorfer, J. *New J. Chem.* **2009**, *33*, 136–147.

(47) Dolzhenko, A. V.; Tan, G. K.; Koh, L. L.; Dolzhenko, A. V.; Chui, W. K. *Acta Crystallogr., Sect. E* **2009**, *65*, o125.

(48) Barker, D. L.; Marsh, R. E. *Acta Crystallogr.* **1964**, *17*, 1581–1587.

(49) (a) Lapinski, L.; Nowak, M. J.; Reva, I.; Rostkowska, H.; Fausto, R. *Phys. Chem. Chem. Phys.* **2010**, *12*, 9615–9618; (b) Lapinski, L.; Reva, I.; Nowak, M. J.; Fausto, R. *Phys. Chem. Chem. Phys.* **2011**, *13*, 9676–9684 and references therein.

(50) Yang, Z.; Rodgers, M. T. *Phys. Chem. Chem. Phys.* **2004**, *6*, 2749–2757.

(51) Ismael, A.; Cristiano, M. L. S.; Fausto, R.; Gómez-Zavaglia, A. *J. Phys. Chem. A* **2010**, *114*, 13076–13085.

(52) Lynch, D. E.; Dougall, T.; Smith, G.; Byriel, K. A.; Kennard, C. H. L. *J. Chem. Crystallogr.* **1999**, *29*, 67–73.

(53) Bugalho, S. C. S.; Serra, A. C.; Lapinski, L.; Cristiano, M. L. S.; Fausto, R. *Phys. Chem. Chem. Phys.* **2002**, *4*, 1725–1731.

(54) Gómez-Zavaglia, A.; Reva, I. D.; Frija, L.; Cristiano, M. L.; Fausto, R. *J. Phys. Chem. A* **2005**, *109*, 7967–7976.

(55) Reva, I. D.; Stepanian, S. G.; Adamowicz, L.; Fausto, R. *Chem. Phys. Lett.* **2003**, *374*, 631–638.

(56) Kurzer, F.; Douraghi-Zadeh, K. *Chem. Rev.* **1967**, *67*, 107–152.

(57) Yranzo, G. I.; Elguero, J.; Flammang, R.; Wentrup, C. *Eur. J. Org. Chem.* **2001**, *12*, 2209–2220.

(58) King, S. T.; Strope, J. H. *J. Chem. Phys.* **1971**, *54*, 1289–1295.

(59) Dendramis, A.; Leroi, G. E. *J. Chem. Phys.* **1977**, *66*, 4334–4340.

(60) Langel, W.; Kollhoff, H.; Knözinger, E. *J. Chem. Phys.* **1989**, *90*, 3430–3442.

(61) Milligan, D. E.; Jacox, M. E. *J. Chem. Phys.* **1967**, *47*, 278–285.